

An Improved Multi-State Constraint Kalman Filter for Visual-Inertial Odometry

M.R. Abdollahi^a, Seid H. Pourtakdoust^b, M.H. Yoosefian Nooshabadi^c and H.N. Pishkenari^c

Abstract—Fast pose estimation (PE) is of vital importance for successful mission performance of agile autonomous robots. Global Positioning Systems such as GPS and GNSS have been typically used in fusion with Inertial Navigation Systems (INS) for PE. However, the low update rate and lack of proper signals make their utility impractical for indoor and urban applications. On the other hand, Visual-Inertial Odometry (VIO) is gaining popularity as a practical alternative for GNSS/INS systems in GPS-denied environments. Among the many VIO-based methods, the Multi-State Constraint Kalman Filter (MSCKF) has received a greater attention due to its robustness, speed and accuracy. To this end, the high computational cost associated with image processing for real-time implementation of MSCKF on resource-constrained vehicles is still a challenging ongoing research. In this paper, an enhanced version of the MSCKF is proposed. To this aim, different feature marginalization and state pruning strategies are suggested that result in a much faster algorithm. The proposed algorithm is tested both on an open-source dataset and in real-world experiments for validation. It is demonstrated that the proposed Fast-MSCKF (FMSCKF) is about six times faster and at least 20% more accurate in final position estimation than the standard MSCKF algorithm.

Index Terms— MSCKF, Fast MSCKF, Visual-Inertial Odometry, Agile Motion, Kalman Filter.

Video Link: https://youtu.be/aE6_av59QXw

I. INTRODUCTION

Accurate and reliable pose estimation is considered as the primary step needed for guidance and controller design of aerial robots. GPS and IMU data fusion has been used for the PE of an autonomous vehicle [1]. However, this method has some drawbacks for some important applications. For instance, satellite signals are not readily available in a variety of places, such as forests, roofed places, and urban areas with high rise buildings. Moreover, the GPS/GNSS update rate is low and with a slight delay. Thus there are many other attempts introduced to replace the GNSS/INS systems and remove their shortcomings. Hybrid utility of camera with IMU is one of the emerging methods for PE, due to their low cost and high quality. The latter is referred to as Visual Inertial Odometry (VIO) in the pertinent literature. VIOs are considered safe, inexpensive and robust replacements for GNSS/INS systems.

VIOs are categorized into two major methods that include

First A. M.R. Abdollahi, PhD Candidate, Department of Aerospace Engineering, Sharif University of Technology, Tehran 14588-89694, Iran, (e-mail: m.abdollahi7466@student.sharif.edu)

Second B. Seid H. Pourtakdoust, (Corresponding Author) Professor, Department of Aerospace Engineering, Sharif University of Technology, Tehran 14588-89694, Iran, (e-mail: pourtak@sharif.edu)

Third C. M.H. Yoosefian Nooshabadi, M.Sc. student, Department of

filter-based and optimization-based as available in the existing literature such as ORB-SLAM [2], SVO+GTSAM [3], CNN-SVO [4], DSO [5], VINS-Mono [6], and Kimera [7]. Optimization-based methods are more accurate for offline or post-processing applications. On the other hand, the real-time accuracy of the filter-based methods is comparable with that of the optimization-based approaches [8].

In some filter-based methods landmark positions are stored in the state vector (see ROVIO [9], EKF- and UKF- SLAM [10]). However, as the number of landmark positions grows, the size of the state vector becomes too large, and thus, the computational cost increases considerably [11]. Therefore, for real-time applications, only a limited number of landmark positions can be used. On the other hand, some filter-based approaches such as MSCKF, store a number of camera poses in the state vector.

The MSCKF was initially introduced by Mourikis et al. [12]. MSCKF uses an Error-State Extended Kalman filter to fuse IMU and camera data and, unlike other KF-based methods, the positions of the landmarks are not stored in the state vector. Instead, a number of recent positions and orientations (i.e., poses) of the camera are kept in the state vector. This alternative reduces the computational cost and increases the accuracy and robustness of PE.

In general, to improve the performance of the VIO algorithms, three main characteristics need to be considered: accuracy, robustness, and speed. There are many studies in the literature that try to enhance and address these three issues. To improve the accuracy, the Patch-based MSCKF [13], which is based on the original MSCKF algorithm, has been developed. Unlike the MSCKF algorithm, which utilizes features (corners), the patch-based MSCKF uses a direct method instead. The accuracy of this algorithm is on average improved by 23% compared to the original MSCKF. In this method, the light intensity of the pixels in distinct patches is used for localization.

Furthermore, Local-Optimal MSCKF (LOMSCKF) has tried to reduce the error of the MSCKF algorithm using nonlinear optimization [3], [14]. The LOMSCKF uses pre-integrated IMU and camera measurements. Moreover, S-MSCKF, which uses a stereo camera instead of a single camera, has enhanced the MSCKF performance. S-MSCKF has shown more

Mechanical Engineering, Sharif University of Technology, Tehran 14588-89694, Iran, (e-mail: m.h.yoosefian@gmail.com)

Fourth D. H.N. Pishkenari, Associate Professor, Department of Mechanical Engineering, Sharif University of Technology, Tehran 14588-89694, Iran, (e-mail: nejat@sharif.edu)

> REPLACE THIS LINE WITH YOUR MANUSCRIPT ID NUMBER (DOUBLE-CLICK HERE TO EDIT) <

robustness with a modest computational cost for fast flight conditions [15].

One of the key drawbacks of the EKF-based methods is the unobservability of the yaw angle. Hence, these methods are inherently inconsistent. Huang has examined this problem and proposed some remedies such as OC-EKF [16] and FEJ-EKF [17]. MA introduced the ACK-MSCKF algorithm [18], which attempts to implement the algorithm for ground-based robots. In this work, the unobservable states of ground robots are investigated and an algorithm is presented to resolve the unobservability problem.

There are also many recent works focusing on the integration of machine learning techniques into visual-inertial navigation for enhanced robustness and accuracy [19], [20]. In this respect, a convolutional neural network has been implemented in the update step of the MSCKF algorithm, which has resulted in higher robustness compared to the original MSCKF in visual-inertial navigation [21].

As discussed above, numerous studies have been conducted on the VIO algorithms, specifically the MSCKF, where most have either tried to improve the accuracy of the algorithms or have attended to the observability issue of the yaw angle. However, there are much fewer studies that have tried to reduce the computational cost of the algorithm. Nonetheless, the high computational cost is the one of the most significant challenges that resource-constrained aerial robots face. So, reducing this computational cost is of a great importance. To this aim, in this paper an attempt is made to reduce the computational cost of the MSCKF algorithm using a new feature management method and the results are compared with the original algorithm.

The rest of the paper is organized as follows: The next section covers the formulation of the MSCKF. In section III the feature management methodology of the original MSCKF and Fast MSCKF, which is the main contribution of this work is presented. The validation results of the implementation of the MSCKF and the new proposed Fast MSCKF on an open-source dataset and in a real-world experiment are shown in section IV. In the next section, a detailed discussion of the results is presented. Finally, conclusions and future research directives are attended to in section VI.

II. THE MULTI STATE CONSTRAINT KALMAN FILTER (MSCKF)

The MSCKF is an error-state extended Kalman filter that can be used to estimate the position and orientation of a camera-IMU system. More precisely, the algorithm estimates the pose of the frame attached to the IMU, $\{I\}$, with respect to a global (reference) frame, $\{G\}$. The state vector of the filter consists of two parts. The first part, which evolves during the propagation step, pertains to the IMU:

$$\mathbf{X}_{IMU} = [{}^I\mathbf{q}_G^T \quad \mathbf{b}_g^T \quad {}^G\mathbf{v}_I^T \quad \mathbf{b}_a^T \quad {}^G\mathbf{p}_I^T]^T \quad (1)$$

in which ${}^I\mathbf{q}_G$ is the unit quaternion indicating the rotation from frame $\{G\}$ to frame $\{I\}$, ${}^G\mathbf{v}_I$ and ${}^G\mathbf{p}_I$ are the velocity and position of the frame $\{I\}$ with respect to and expressed in frame

$\{G\}$, and \mathbf{b}_g and \mathbf{b}_a are gyroscope and accelerometer biases, respectively. The second part of the state vector includes a number of poses of the camera frames $\{C\}$ with respect to the global frame $\{G\}$. This part is added to the state vector during the augmentation process (section II.B). The algorithm comprises three steps, which are explained in the following sections.

A. The propagation step

Every time a new IMU measurement is received, the first part of the state vector that is related to the IMU, and its corresponding covariance matrix propagate. Considering a calibrated IMU (i.e., misalignment, temperature effect, scale-factor, etc. are compensated), the measurement models for the gyroscope and the accelerometer are:

$$\boldsymbol{\omega}_m = \boldsymbol{\omega} + \mathbf{b}_g + \mathbf{n}_g \quad (2)$$

$$\mathbf{a}_m = {}^I\mathbf{R}_G({}^G\mathbf{a} - {}^G\mathbf{g}) + \mathbf{b}_a + \mathbf{n}_a \quad (3)$$

in which $\boldsymbol{\omega}_m$ and $\boldsymbol{\omega}$ are the measured and true angular velocities, \mathbf{a}_m is the measured body acceleration, ${}^I\mathbf{R}_G$ is the rotation matrix corresponding to the quaternion ${}^I\mathbf{q}_G$, \mathbf{n}_g and \mathbf{n}_a are zero mean white process noise vectors, ${}^G\mathbf{a}$ is the acceleration of frame $\{I\}$ expressed in $\{G\}$, and ${}^G\mathbf{g}$ is the local gravity vector expressed in $\{G\}$. The biases are modelled as the random walk process, so the time derivatives of elements of the IMU state vector will be:

$${}^I\dot{\mathbf{q}}_G(t) = \frac{1}{2}\boldsymbol{\Omega}(\boldsymbol{\omega}(t)){}^I\mathbf{q}_G(t) \quad (4)$$

$$\dot{\mathbf{b}}_g(t) = \mathbf{n}_{wg}(t) \quad (5)$$

$${}^G\dot{\mathbf{v}}_I(t) = {}^G\mathbf{a}(t) \quad (6)$$

$$\dot{\mathbf{b}}_a(t) = \mathbf{n}_{wa}(t) \quad (7)$$

$${}^G\dot{\mathbf{p}}_I(t) = {}^G\mathbf{v}_I(t) \quad (8)$$

In these equations, \mathbf{n}_{wg} and \mathbf{n}_{wa} are random walk noise vectors and

$$\boldsymbol{\Omega}(\boldsymbol{\omega}) = \begin{bmatrix} -[\boldsymbol{\omega} \times] & \boldsymbol{\omega}^T \\ -\boldsymbol{\omega} & 0 \end{bmatrix}, \quad [\boldsymbol{\omega} \times] = \begin{bmatrix} 0 & -\omega_z & \omega_y \\ \omega_z & 0 & -\omega_x \\ -\omega_y & \omega_x & 0 \end{bmatrix} \quad (9)$$

Applying the expectation operator on the equations (4) to (8) yields:

$${}^I\hat{\mathbf{q}}_G = \frac{1}{2}\boldsymbol{\Omega}(\hat{\boldsymbol{\omega}}){}^I\mathbf{q}_G \quad (10)$$

$$\dot{\hat{\mathbf{b}}}_g = \mathbf{0} \quad (11)$$

$${}^G\hat{\mathbf{v}}_I = {}^I\hat{\mathbf{R}}_G^T \hat{\mathbf{a}} + {}^G\mathbf{g} \quad (12)$$

$$\dot{\hat{\mathbf{b}}}_a = \mathbf{0} \quad (13)$$

$${}^G\hat{\mathbf{p}}_I = {}^G\hat{\mathbf{v}}_I \quad (14)$$

> REPLACE THIS LINE WITH YOUR MANUSCRIPT ID NUMBER (DOUBLE-CLICK HERE TO EDIT) <

where $\widehat{\boldsymbol{\omega}} = \boldsymbol{\omega}_m - \widehat{\boldsymbol{b}}_g$ and $\widehat{\boldsymbol{a}} = \boldsymbol{a}_m - \widehat{\boldsymbol{b}}_a$. These equations can be solved either by continuous-time integration (using differential equations) or discrete-time (using Runge-Kutta methods, for instance) integration to get the IMU state propagation equations. The covariance matrix needs to be propagated as well. This matrix, at time $k+1$, can be partitioned as:

$$\mathbf{P}_{k+1|k} = \begin{bmatrix} \mathbf{P}_{II_{k+1|k}} & \mathbf{P}_{IC_{k+1|k}} \\ \mathbf{P}_{CI_{k+1|k}} & \mathbf{P}_{CC_{k|k}} \end{bmatrix} \quad (15)$$

in which the $\mathbf{P}_{II_{k+1|k}}$ is the covariance related to the IMU state variables (the correlation between IMU state variables) and can be calculated through numerical integration of the following Lyapunov equation:

$$\dot{\mathbf{P}}_{II} = \mathbf{F}\mathbf{P}_{II} + \mathbf{P}_{II}\mathbf{F}^T + \mathbf{G}\mathbf{Q}_I\mathbf{G}^T \quad (16)$$

in which

$$\mathbf{F} = \begin{bmatrix} -[\widehat{\boldsymbol{\omega}} \times] & -\mathbf{I}_3 & \mathbf{0} & \mathbf{0} & \mathbf{0} \\ \mathbf{0} & \mathbf{0} & \mathbf{0} & \mathbf{0} & \mathbf{0} \\ -{}^G\widehat{\mathbf{R}}_I[\widehat{\boldsymbol{a}} \times] & \mathbf{0} & \mathbf{0} & -{}^G\widehat{\mathbf{R}}_I & \mathbf{0} \\ \mathbf{0} & \mathbf{0} & \mathbf{0} & \mathbf{0} & \mathbf{0} \\ \mathbf{0} & \mathbf{0} & \mathbf{I}_3 & \mathbf{0} & \mathbf{0} \end{bmatrix} \quad (17)$$

$$\mathbf{G} = \begin{bmatrix} -\mathbf{I}_3 & \mathbf{0} & \mathbf{0} & \mathbf{0} \\ \mathbf{0} & \mathbf{I}_3 & \mathbf{0} & \mathbf{0} \\ \mathbf{0} & \mathbf{0} & -{}^G\widehat{\mathbf{R}}_I & \mathbf{0} \\ \mathbf{0} & \mathbf{0} & \mathbf{0} & \mathbf{I}_3 \\ \mathbf{0} & \mathbf{0} & \mathbf{0} & \mathbf{0} \end{bmatrix} \quad (18)$$

and \mathbf{Q}_I is the covariance matrix corresponding to the noise vector:

$$\mathbf{n}_I = [\mathbf{n}_g^T \quad \mathbf{n}_{wg}^T \quad \mathbf{n}_a^T \quad \mathbf{n}_{wa}^T]^T \quad (19)$$

The next term in the covariance matrix is $\mathbf{P}_{IC_{k+1|k}}$, which is the correlation between the IMU and the camera measurements and is propagated using:

$$\mathbf{P}_{IC_{k+1|k}} = \Phi(t_k + T, t_k)\mathbf{P}_{IC_{k|k}} \quad (20)$$

in which T is the sampling time of the IMU and Φ is the state transition matrix that evolves over time with the following equation:

$$\dot{\Phi}(t_k + \tau, t_k) = \mathbf{F}\Phi(t_k + \tau, t_k), \quad \tau \in [0, T] \quad (21)$$

B. The augmentation step

Upon recording an image, the camera pose is calculated using the most recent estimation of the IMU pose. Assume that the filter is currently at $(k+1)th$ step and the state vector already includes l number of camera poses. When the $(l+1)th$ image is received, its poses are calculated using:

$${}^{c_{l+1}}\widehat{\mathbf{q}}_G = {}^c\mathbf{q}_I \otimes {}^{I_{k+1}}\widehat{\mathbf{q}}_G \quad (22)$$

$${}^c\widehat{\mathbf{p}}_{c_{l+1}} = {}^G\widehat{\mathbf{p}}_{I_{k+1}} + {}^G\widehat{\mathbf{R}}_{I_{k+1}}{}^I\mathbf{p}_C \quad (23)$$

in which ${}^I\mathbf{p}_C$ and ${}^c\mathbf{q}_I$ are translation vector and quaternion between the IMU frame and the camera frame. Since these two sensors are rigidly attached to each other ${}^I\mathbf{p}_C$ and ${}^c\mathbf{q}_I$ are constant and thus can be computed in an offline calibration procedure. Now the state vector can be augmented as:

$$\widehat{\mathbf{X}}_{aug} = [\widehat{\mathbf{X}}^T \quad {}^{c_{l+1}}\widehat{\mathbf{q}}_G^T \quad {}^G\widehat{\mathbf{p}}_{c_{l+1}}^T]^T \quad (24)$$

in which $\widehat{\mathbf{X}}$ is the state vector prior to augmentation. In addition to the state vector, the covariance matrix should also be augmented as:

$$\mathbf{P} = \begin{bmatrix} \mathbf{I}_{6l+15} \\ \mathbf{J} \end{bmatrix} \mathbf{P} \begin{bmatrix} \mathbf{I}_{6l+15} \\ \mathbf{J} \end{bmatrix}^T \quad (25)$$

in which \mathbf{J} is the Jacobian matrix that is calculated using (22) and (23) as:

$$\mathbf{J} = \begin{bmatrix} {}^c\mathbf{R}_I & \mathbf{0}_{3 \times 9} & \mathbf{0}_{3 \times 3} & \mathbf{0}_{3 \times 6l} \\ [{}^G\mathbf{R}_{I_{k+1}} {}^I\mathbf{p}_C \times] & \mathbf{0}_{3 \times 9} & \mathbf{I}_3 & \mathbf{0}_{3 \times 6l} \end{bmatrix} \quad (26)$$

C. The Update step

The filter update step is done using a number of features extracted from some images (whose poses are available in the state vector). The policy based on which these features are chosen is the subject of the next section and is the key distinction between the proposed method and the original MSCKF algorithm. Assume m number of features are observed in n_j number of images ($l - n_j, \dots, l - 1$). Each image consists of pixel coordinates of different features. So, the camera measurement model for the j -th ($j = 1, \dots, m$) feature observed in the i -th ($i = 1, \dots, n_j$) frame is:

$${}^c_i\mathbf{z}_{f_j} = \frac{1}{c_i Z_{f_j}} \begin{bmatrix} c_i X_{f_j} \\ c_i Y_{f_j} \\ c_i Z_{f_j} \end{bmatrix} + {}^c_i\mathbf{n}_{f_j} \quad (27)$$

in which ${}^c_i\mathbf{n}_{f_j}$ is the measurement noise vector with ${}^c_i\mathbf{R}_{f_j} = \sigma_{im}^2 \mathbf{I}_2$ as its covariance matrix and ${}^c_i\mathbf{p}_{f_j} = [{}^c_i X_{f_j} \quad {}^c_i Y_{f_j} \quad {}^c_i Z_{f_j}]^T$ is the position of the j -th feature in the i -th camera frame. Using all n_j measurements of the feature, it is possible to compute an estimation of the feature position in the $\{G\}$ frame through a triangulation process (e.g., as in [22], [23]). Assume that the estimated position of the j -th feature in the global frame is ${}^G\widehat{\mathbf{p}}_{f_j}$. Now, the estimate of the j -th feature position in the i -th image is calculated via:

$${}^c_i\widehat{\mathbf{p}}_{f_j} = {}^c_i\widehat{\mathbf{R}}_G ({}^G\widehat{\mathbf{p}}_{f_j} - {}^G\widehat{\mathbf{p}}_{c_i}) = \begin{bmatrix} {}^c_i \widehat{X}_{f_j} \\ {}^c_i \widehat{Y}_{f_j} \\ {}^c_i \widehat{Z}_{f_j} \end{bmatrix} \quad (28)$$

and using the measurement of the feature, the residual is calculated:

$${}^c_i\mathbf{r}_{f_j} = {}^c_i\mathbf{z}_{f_j} - {}^c_i\widehat{\mathbf{z}}_{f_j} \quad (29)$$

in which

> REPLACE THIS LINE WITH YOUR MANUSCRIPT ID NUMBER (DOUBLE-CLICK HERE TO EDIT) <

$${}^c_i \hat{\mathbf{z}}_{f_j} = \frac{1}{{}^c_i \hat{Z}_{f_j}} \begin{bmatrix} {}^c_i \hat{X}_{f_j} & {}^c_i \hat{Y}_{f_j} \end{bmatrix}^T \quad (30)$$

Subsequently, the Jacobians of the measurement model with respect to the feature position (${}^c_i \mathbf{H}_{f_j}$) and state vector (${}^c_i \mathbf{H}_{X_j}$) are calculated:

$${}^c_i \mathbf{H}_{f_j} = {}^c_i \mathbf{J}_{f_j} {}^c_i \hat{\mathbf{R}}_G \quad (31)$$

$$\begin{aligned} {}^c_i \mathbf{H}_{X_j} &= \begin{bmatrix} {}^c_i \mathbf{H}_{X_j} & \dots & {}^c_i \mathbf{H}_{f_j} \end{bmatrix} \begin{bmatrix} ({}^c_i \hat{\mathbf{p}}_{f_j} - {}^c_i \hat{\mathbf{p}}_{c_i}) \times & -{}^c_i \mathbf{H} \end{bmatrix} \quad (32) \\ &= \begin{bmatrix} \mathbf{0}_{2 \times 15} & \dots & {}^c_i \mathbf{H}_{f_j} \end{bmatrix} \begin{bmatrix} ({}^c_i \hat{\mathbf{p}}_{f_j} - {}^c_i \hat{\mathbf{p}}_{c_i}) \times & -{}^c_i \mathbf{H} \end{bmatrix} \end{aligned}$$

in which

$${}^c_i \mathbf{J}_{f_j} = \left(\frac{1}{{}^c_i \hat{Z}_{f_j}} \right)^2 \begin{bmatrix} {}^c_i \hat{Z}_{f_j} & 0 & -{}^c_i \hat{X}_{f_j} \\ 0 & {}^c_i \hat{Z}_{f_j} & -{}^c_i \hat{Y}_{f_j} \end{bmatrix} \quad (33)$$

The above calculations are done for all n_j images, in which the j -th feature is observed. Concatenating all calculations for the feature gives:

$$\mathbf{r}_{f_j} = \begin{bmatrix} {}^c_1 \mathbf{r}_{f_j}^T & \dots & {}^c_{n_j} \mathbf{r}_{f_j}^T \end{bmatrix}^T \quad (34)$$

$$\mathbf{H}_{f_j} = \begin{bmatrix} {}^c_1 \mathbf{H}_{f_j}^T & \dots & {}^c_{n_j} \mathbf{H}_{f_j}^T \end{bmatrix}^T \quad (35)$$

$$\mathbf{H}_{X_j} = \begin{bmatrix} {}^c_1 \mathbf{H}_{X_j}^T & \dots & {}^c_{n_j} \mathbf{H}_{X_j}^T \end{bmatrix}^T \quad (36)$$

Now, let \mathbf{A}_{f_j} be the left null-space of \mathbf{H}_{f_j} , then:

$$\mathbf{H}_{o_j} = \mathbf{A}_{f_j}^T \mathbf{H}_{X_j} \quad (37)$$

$$\mathbf{R}_{o_j} = \sigma_{im}^2 \mathbf{A}_{f_j}^T \mathbf{A}_{f_j} \quad (38)$$

$$\mathbf{r}_{o_j} = \mathbf{A}_{f_j}^T \mathbf{r}_{f_j} \quad (39)$$

\mathbf{H}_{o_j} , \mathbf{R}_{o_j} , and \mathbf{r}_{o_j} are calculated for all m features which are selected to be used to do the filter update. Stacking these calculated matrices will give:

$$\mathbf{H}_o = [\mathbf{H}_{o_1} \dots \mathbf{H}_{o_m}] \quad (40)$$

$$\mathbf{r}_o = [\mathbf{r}_{o_1} \dots \mathbf{r}_{o_m}] \quad (41)$$

$$\mathbf{R}_o = \text{diag}(\mathbf{R}_{o_1}, \dots, \mathbf{R}_{o_m}) \quad (42)$$

where $\mathbf{r}_o \in \mathbb{R}^{d \times 1}$ is the final residual computed for all m features seen in n_j images, with:

$$d = \sum_{j=1}^m (2n_j - 3)$$

Since the number of features can be large, an extra step can be taken in order to reduce the computational cost. More specifically, reduced QR decomposition is utilized to decompose the \mathbf{H}_o matrix as:

$$\mathbf{H}_o = [\mathbf{Q}_1 \quad \mathbf{Q}_2] \begin{bmatrix} \mathbf{T}_H \\ \mathbf{0} \end{bmatrix} \quad (43)$$

where \mathbf{Q}_1 and \mathbf{Q}_2 are unitary matrices and \mathbf{T}_H is an upper triangular matrix. As a result, the calculated matrices in (40) to (42) can be reduced to:

$$\mathbf{H}_n = \mathbf{T}_H \quad (44)$$

$$\mathbf{r}_n = \mathbf{Q}_1^T \mathbf{r}_o \quad (45)$$

$$\mathbf{R}_n = \mathbf{Q}_1^T \mathbf{R}_o \mathbf{Q}_1 \quad (46)$$

Now, the Kalman gain can be computed:

$$\mathbf{S} = \mathbf{H}_n \mathbf{P}_{k+1|k} \mathbf{H}_n^T \quad (47)$$

$$\mathbf{K} = \mathbf{P}_{k+1|k} \mathbf{H}_n^T \mathbf{S}^{-1} \quad (48)$$

This gain is next used to update the state vector and the covariance matrix:

$$\mathbf{P}_{k+1|k+1} = \mathbf{P}_{k+1|k} - \mathbf{K} \mathbf{S} \mathbf{K}^T \quad (49)$$

$$\tilde{\mathbf{X}} = \mathbf{K} \mathbf{r}_n \quad (50)$$

$$\tilde{\mathbf{X}}_{k+1|k+1} = \tilde{\mathbf{X}}_{k+1|k} \oplus \tilde{\mathbf{X}} \quad (51)$$

in which the \oplus sign is the general form of addition, which for the quaternion elements is equivalent to quaternion multiplication and for other elements is the same as normal addition. The calculated state vector and covariance matrix will then be used for the next propagation step.

III. FEATURE MARGINALIZATION AND STATE PRUNING

In the previous section, it was assumed that m number of features are used to perform the update step of the MSCKF algorithm. In this section, the approach used to select these features is explained. In the conventional MSCKF, the update step is carried out when at least one feature is no longer visible or when the number of camera poses available in the state vector reaches its maximum, $N_{p,\max}$. In the former case that happens most often, whenever a new image is received, there are some features that have gone outside of the field of view, and therefore, cannot be tracked (unless the camera is not moving). These features are selected and used to do the update. Additionally, the same number of features as those that are no longer observed should be extracted from the new image. When all features of an image are already used in the update step, it no longer contains useful information, so its corresponding pose is removed from the state vector. Moreover, its corresponding row and column in the covariance matrix are also removed. As a result, the state vector and the covariance matrix are pruned and do not grow unbounded. The latter case happens when the camera does not move fast enough such that although some features may fall outside the view, and are used to carry out the filter update, the state vector and the covariance matrix are not

> REPLACE THIS LINE WITH YOUR MANUSCRIPT ID NUMBER (DOUBLE-CLICK HERE TO EDIT) <

pruned. So, eventually, the number of stored camera poses reaches its maximum. In this case, at least one image should be removed. Before removing that image, all its features and their tracks in the preceding images are used to do an update. Then, the image along with its elements in the state vector and covariance matrix is removed. Instead of removing only one image, in the original MSCKF, $N_{p,max}/3$ number of images are removed. So, the tuning parameter in the conventional MSCKF is $N_{p,max}$. On the other hand, in Fast MSCKF we propose an extra case that is based on the minimum number of features. In this case, contrary to the conventional MSCKF, where features were extracted from all images, features are only extracted from some images that will be referred to as the keyframes.

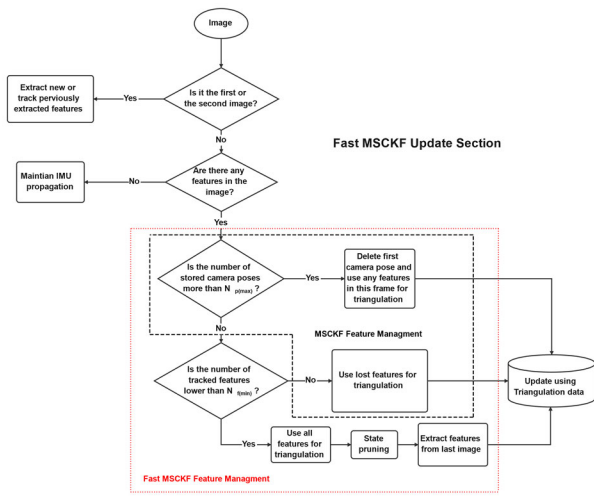


Fig. 1. A flowchart of MSCKF and Fast MSCKF feature management approaches.

More specifically, in this approach, after extracting features from a keyframe, these features are tracked and no new features are extracted until the number of tracked features falls below a certain number, $N_{f,min}$. All these feature tracks are then used to do an update. Then all images, except the last image (the keyframe) are removed and the state vector and covariance matrix are pruned accordingly. The last image is then used to extract new features to be tracked in future images. Therefore, in the proposed strategy three cases are possible to trigger the filter update. The first case happens when at least one feature goes outside the field of view.

This case happens most of the time. The second case happens when the number of tracked features falls below a minimum value, $N_{f,min}$. Lastly, the third case occurs when the number of poses available in the state vector exceeds a maximum number, $N_{p,max}$. This method is proved to be much faster and more accurate than the original approach in practice. A schematic of these two feature management methods is shown in Figure 1. In the next section, the two mentioned methods are critically examined. The discussion about the performance of these approaches is presented in the discussion section. The pseudocode of the update step of the proposed Fast MSCKF is presented in Algorithm 1.

Algorithm 1. Fast MSCKF Pseudocode

Input: Augmented state vector, augmented covariance matrix, m features tracked in n_j images

Output: Updated state vector and covariance matrix

1 **For** $j = 1, \dots, m$ **do:**

2 **Calculate** the position of the j -th feature in the global frame using triangulation methods.

3 **For** $i = l - n, \dots, l - 1$ **do:**

4 **Calculate** the position of the j -th feature in the i -th frame using equation (28)

5 **Estimate** the measurement using (30) and using normalized measurement (from the camera) calculate the residual using (29)

6 **Use** (31), (32) and (33) to calculate $c_i \mathbf{H}_{f_j}$, $c_i \mathbf{H}_{X_j}$, and $c_i \mathbf{J}_{f_j}$

7 **End**

8 **Use** (34) to (36) to compute \mathbf{r}_{f_j} , \mathbf{H}_{f_j} and \mathbf{H}_{X_j}

9 **Calculate** the left null-space of \mathbf{H}_{f_j}

10 **Calculate** \mathbf{H}_{o_j} , \mathbf{r}_{o_j} and \mathbf{R}_{o_j} using (37) to (39)

11 **Perform** a Mahalanobis gating test to reject the outliers

12 **End**

13 **Calculate** \mathbf{H}_o , \mathbf{r}_o and \mathbf{R}_o using (40) to (42)

14 **Perform** QR decomposition and calculate \mathbf{H}_n , \mathbf{H}_n and \mathbf{H}_n using (44) to (46)

15 **Update** covariance matrix and state vector using (49) and (51)

Table I

RESULTS OF RUNNING ALGORITHMS ON EUROC [24] DATASET, ON THE PERSONAL LAPTOP. THE FINAL POINT ERROR IS CALCULATED WITH RESPECT TO THE TRAVELED DISTANCE

| Method | Final x (m) | Final y (m) | Final z (m) | Final point error (%) | Final ϕ (°) | Final θ (°) | Final ψ (°) | Final orientation error (°) | Update rate (Hz) |
|---------------------|-------------|-------------|-------------|-----------------------|------------------|--------------------|------------------|-----------------------------|------------------|
| ROVIO | 4.35 | -2.10 | 0.23 | 0.57 | -2.73 | -2.01 | -21.61 | 2.09 | 15 |
| SVO (VIO) | 4.93 | -2.27 | 0.73 | 0.98 | -6.42 | 0.32 | -21.89 | 4.86 | 12 |
| SVO+GTSAM | 4.89 | -1.92 | 0.76 | 0.49 | -2.55 | -1.07 | -22.82 | 1.59 | 25 |
| MSCKF | 4.82 | -1.51 | 0.83 | 0.49 | -2.24 | -1.53 | -23.51 | 1.52 | 11 |
| Fast MSCKF | 4.54 | -1.78 | 0.76 | 0.25 | -2.4 | -1.44 | -22.44 | 1.39 | 70 |
| Ground Truth | 4.66 | -1.80 | 0.64 | -- | -2.32 | -1.63 | -25.90 | -- | -- |

IV. RESULTS

In this section, the results of the proposed algorithm are presented. For the original MSCKF, the maximum allowable number of poses is set to $N_{p,\max} = 20$, and for our proposed method, the minimum number of allowable features is set to $N_{f,\min} = 8$ and similar to the original MSCKF the maximum allowable number of poses is set to $N_{p,\max} = 20$. For keyframes, in which corners need to be extracted, at most 350 Harris corners are detected and tracked in consecutive frames. A KLT [25] algorithm is then used to track the detected features. To remove wrongly tracked features (outlier rejection) RANSAC [26] is used.

A. Public dataset

The EuRoC MAV dataset [24] (Machine Hall 01) is used to implement the algorithm. To have a more general comparison, the results of SVO (VIO) [27], SVO+GTSAM [3], and ROVIO [9] algorithms are also presented. For these two algorithms, the default settings are used. All algorithms were executed on a personal laptop with a Core i5-4200U CPU and 4 GB RAM. The position and orientation estimation results are shown in Figures 2 to 6.

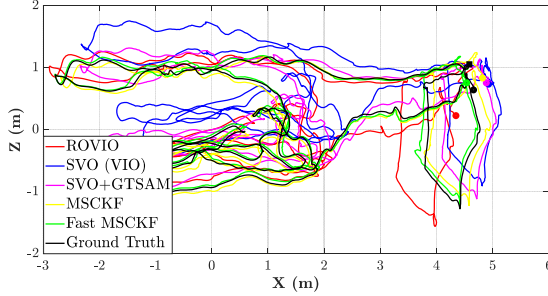


Fig. 2. Ground-truth trajectory (black) in XZ plane, along with the estimated trajectories using various algorithms. The initial position is indicated with a black square while final points are indicated using circles.

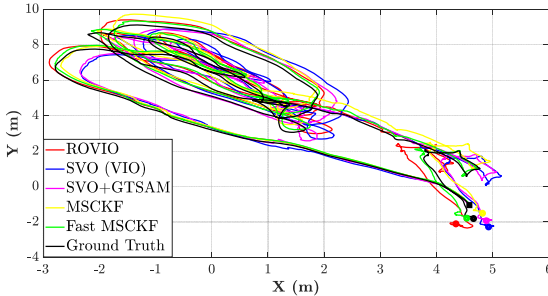


Fig. 3. Ground-truth trajectory (black) in XY plane, the estimated trajectories using ROVIO (red), SVO (VIO) (blue), SVO+GTSAM (magenta), conventional MSCKF (yellow), and Fast MSCKF (green). The starting point is indicated with a black square while final points are indicated using circles.

Also, the Root Mean Square Error (RMSE) of the position and orientation estimation are shown in Figures 7 and 8. From Figure 7, it is obvious that Fast MSCKF outperforms all the other algorithms in orientation estimation. One should note that the ascending behavior of orientation error in Figure 7 is due to the fact that in EKF-based visual-inertial

estimators the yaw angle is not observable [28] and therefore, it drifts over time. From Figure 8 it can be deduced that Fast MSCKF has a lower error in position estimation compared to other algorithms. The results presented in this section are also summarized in Table I.

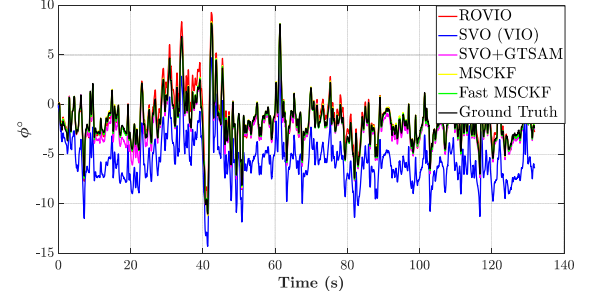


Fig. 4. Ground-truth roll (black) and the estimated roll using ROVIO (red), SVO (VIO) (blue), SVO+GTSAM (magenta), conventional MSCKF (yellow), and Fast MSCKF (green).

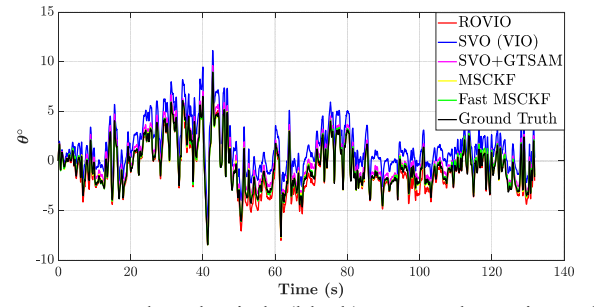


Fig. 5. Ground-truth pitch (black) versus the estimated pitch using ROVIO (red), SVO (VIO) (blue), SVO+GTSAM (magenta), conventional MSCKF (yellow), and Fast MSCKF (green).

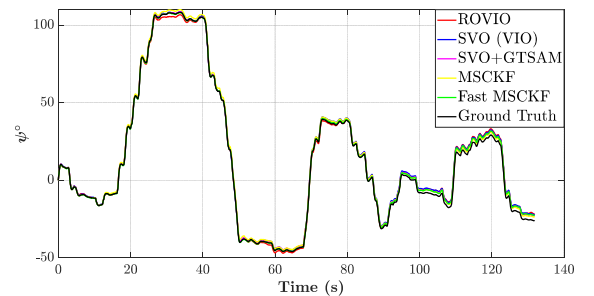


Fig. 6. Ground-truth yaw (black) versus the estimated yaw using ROVIO (red), SVO (VIO) (blue), SVO+GTSAM (magenta), conventional MSCKF (yellow), and Fast MSCKF (green).

The frame processing time (the time span between the moment an image is recorded and the moment that the update and state pruning steps are done) versus run time is shown in Figure 9. As expected, the Fast MSCKF processes the frames much faster than the original MSCKF. The average time that it takes for the proposed Fast MSCKF to process a frame is about 250 (ms) and for the original MSCKF is approximately 1400 (ms).

> REPLACE THIS LINE WITH YOUR MANUSCRIPT ID NUMBER (DOUBLE-CLICK HERE TO EDIT) <

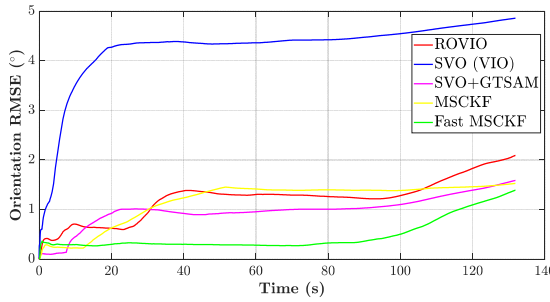


Fig. 7. RMSE of orientation estimation for different algorithms used in this paper.

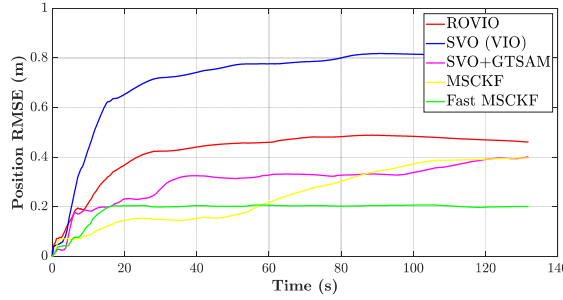


Fig. 8. RMSE of position estimation for different algorithms used in this paper.

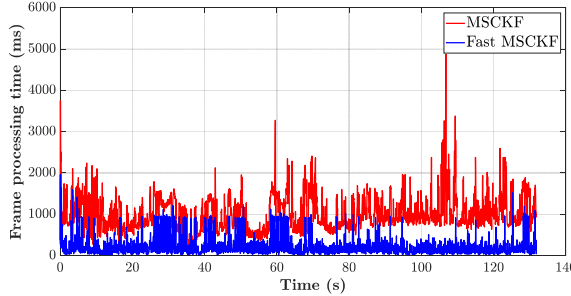


Fig. 9. Frame Processing time for Fast MSCKF (blue) and MSCKF (red).

B. Real-world experiment

An experimental setup was fabricated and utilized to test the proposed algorithm as well. An NVIDIA Jetson Xavier NX was used as the main processor. The setup is shown in Figure 10. Additional information about the sensors used in the platform is provided in Table II. The setup was calibrated using Kalibr [29]. To have a better and explicit comparison, only the original MSCKF and the proposed Fast MSCKF were used for this experiment. The filters were not executed in real-time, but the acquired data was subsequently used on the personal laptop to run the filters.

Table II

SENSOR SETUP

| Sensor | Type | Rate (Hz) |
|--------------|------------------------|-----------|
| ADIS 16467-2 | MEMS IMU | 100 |
| Raspberry Pi | Rolling shutter camera | 10 |
| Camera V2 | | |

In the experiment, a 45 meters-long trajectory was traversed in approximately 90 seconds. A sample image recorded during this experiment is shown in Figure 11.

Since the ground-truth trajectory was not available, in order to evaluate the performance of the two algorithms, we

tried to make a loop and return exactly to the starting point, such that we can measure and compare the final point error for each algorithm. The estimated trajectories are shown in Figures 12 and 13. As it can be seen from both Figures 12 and 13, both algorithms have a good performance in position estimation. It is worthy to mention that the difference in the estimated trajectories of the two algorithms is mostly due to the low quality of the camera.

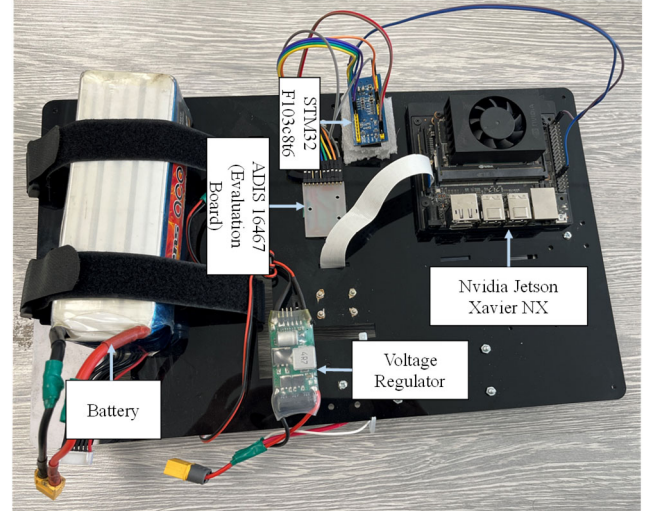


Fig. 10. Back view of the test setup. The camera is mounted on the front side. STM32 F103c8t6 receives data from the ADIS and after a preprocessing process sends them to the Nvidia Jetson board.



Fig. 11. A sample image of our private dataset.

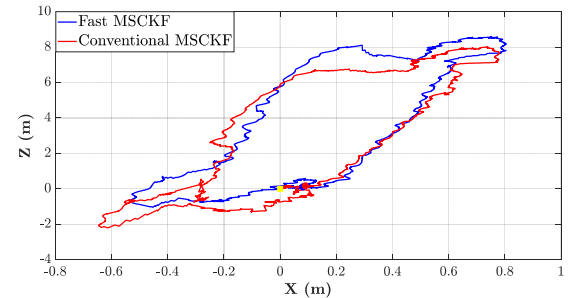


Fig. 12. Estimated trajectory in XZ plane using Fast MSCKF (blue) and conventional MSCKF (red). The starting point is indicated by a yellow square and final points are marked with circles.

> REPLACE THIS LINE WITH YOUR MANUSCRIPT ID NUMBER (DOUBLE-CLICK HERE TO EDIT) <

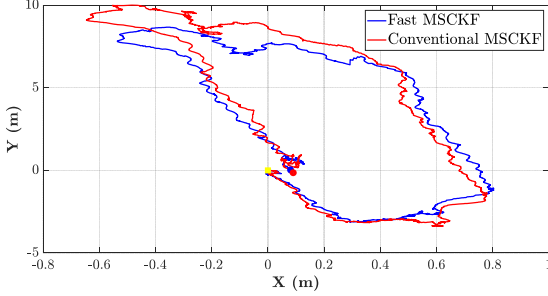


Fig. 13. Estimated trajectory in XY plane using Fast MSCKF (blue) and conventional MSCKF (red). The initial point is marked with a yellow square and final points are represented by circles.

The final location of the two algorithms as well as the ground-truth final position are:

$$\begin{aligned}\mathbf{p}_F &= [0.0806 \quad 0.0355 \quad 0.1085]^T \\ \mathbf{p}_C &= [0.0899 \quad -0.1385 \quad 0.1747]^T \\ \mathbf{p}_{GT} &= [0 \quad 0 \quad 0]^T\end{aligned}$$

Accordingly, the final point error for the proposed Fast MSCKF is 0.14 (m), and for the original MSCKF is 0.24 (m). In other words, for the 45 meters-long trajectory, the final point error of the Fast MSCKF is 0.31% and the error of the original MSCKF is 0.53% of the traveled distance. These errors are in good compliance with the final point errors of the algorithms running on the EuRoC MAV dataset (fifth column of Table I). Estimated velocities and biases are shown in Figures 14 to 16. In these figures, dashed plots are the results of the original MSCKF while the solid plots correspond to the proposed Fast MSCKF.

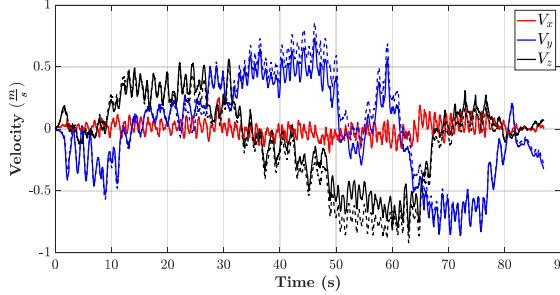


Fig. 14. Estimated velocities during the experiment using Fast MSCKF (solid) and original MSCKF (dashed)

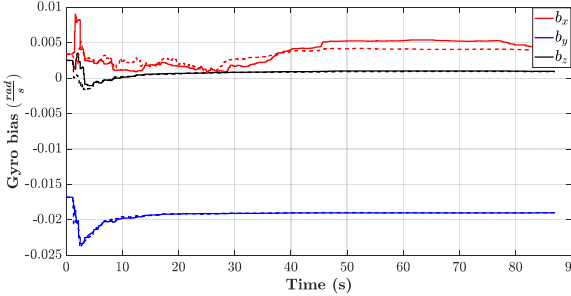


Fig. 15. Estimated gyroscope biases during the experiment using Fast MSCKF (solid) and original MSCKF (dashed)

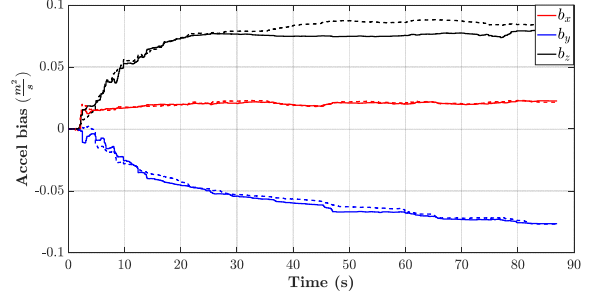


Fig. 16. Estimated accelerometer biases during the experiment using Fast MSCKF (solid) and original MSCKF (dashed)

V. DISCUSSION

The results in the previous section showed that the Fast MSCKF is both faster and more accurate against the original MSCKF. This superiority is to be explained in this section. There are two reasons for the higher update rate. Firstly, the second scenario in Fast MSCKF, where the number of features reaches its minimum, happens more often than the third one. As a result, the state vector and the covariance matrix in our method are pruned more often than in the original version, thus making the algorithm faster. Secondly, in the conventional MSCKF features are extracted from all frames, but in the Fast MSCKF features are only extracted from the keyframes, when the number of tracked features is less than $N_{f,min}$. So, the image processing cost is considerably reduced in Fast MSCKF.

As shown in the previous section, the accuracy of our approach in orientation estimation is comparable with MSCKF, but in position estimation is better than that of the original MSCKF. The reason for the higher accuracy in position in Fast MSCKF is also twofold. Firstly, the rate at which the update occurs in the Fast MSCKF is higher compared to the original MSCKF. To delineate, as mentioned in section II.B, in the augmentation step, camera poses are calculated using the propagated IMU states. We know that the propagated states drift quickly as IMU readings are integrated in that step (i.e., dead reckoning). As a result, the longer the filter delays the update step, the less accurate camera poses will become, and therefore the less accurate the triangulated points will be. Secondly, in the Fast MSCKF, when the number of tracked features falls below $N_{f,min}$, a relatively large number of features ($N_{f,min}$) are used to do the update. Hence, the updated states are more accurate. This event does not happen in the original MSCKF.

As discussed earlier, $N_{f,min}$ is a tuning parameter and must be set appropriately. Setting $N_{f,min}$ to high values causes high state pruning rates, and therefore, the algebraic computation cost reduces. However, high values of $N_{f,min}$ increases feature extraction frequency, which leads to a significantly high image processing cost. Our tests showed that algebraic cost constitutes only 10% of the whole computational cost, and the other 90% pertains to the image processing part. Moreover, the lower the $N_{f,min}$, the higher

the accuracy, because when the number of minimum features is low, the filter has more information about one feature (resulted from consecutive images). In other words, when the number of frames in which a feature is observed is higher, the filter has further information about that feature, and therefore, the triangulated point corresponding to that feature can be more accurate. As a result of the above discussion, it can be concluded that: The lower the $N_{f,min}$ is set, the higher both the update rate and the accuracy will be. To prove the above-mentioned claim in practice, we analyzed the performance of Fast MSCKF under different values of $N_{f,min}$ on the first 10 seconds of the EuRoC MAV dataset [24]. We calculated the “position error to output rate” ratio for different values of $N_{f,min}$ and fitted a curve to them. The obtained plot is shown in Figure 17. In accordance with our assertion, it is obvious from Figure 17 that when a higher $N_{f,min}$ is used, the error to speed ratio is higher.

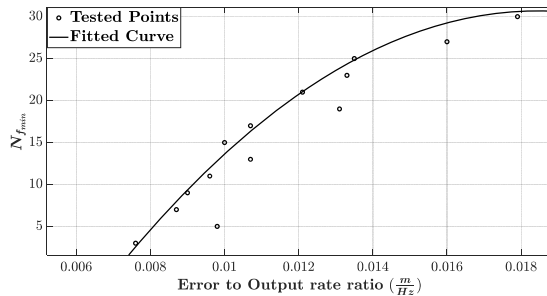


Fig. 17. The effect of $N_{f,min}$ on the error to speed ratio in Fast MSCKF

It is also worthy to note that the performance of the proposed algorithm improves in agile motions. This is because when the robot moves faster, features fall out of the field of view faster, and the update step occurs more often.

REFERENCES

- [1] S. Sukkarieh, E. M. Nebot, and H. F. Durrant-Whyte, ‘A high integrity IMU/GPS navigation loop for autonomous land vehicle applications’, *IEEE Transactions on Robotics and Automation*, vol. 15, no. 3, pp. 572–578, Jun. 1999, doi: 10.1109/70.768189.
- [2] R. Mur-Artal, J. M. M. Montiel, and J. D. Tardos, ‘ORB-SLAM: A Versatile and Accurate Monocular SLAM System’, *IEEE Transactions on Robotics*, vol. 31, no. 5, pp. 1147–1163, Oct. 2015, doi: 10.1109/TRO.2015.2463671.
- [3] C. Forster, L. Carlone, F. Dellaert, and D. Scaramuzza, ‘On-Manifold Preintegration for Real-Time Visual-Inertial Odometry’. [Online]. Available: <https://youtu.be/CsJkci5lfco>
- [4] S. Y. Loo, A. J. Amiri, S. Mashohor, S. H. Tang, and H. Zhang, ‘CNN-SVO: Improving the Mapping in Semi-Direct Visual Odometry Using Single-Image Depth Prediction’, Oct. 2018, [Online]. Available: <http://arxiv.org/abs/1810.01011>
- [5] J. Engel, V. Koltun, and D. Cremers, ‘Direct Sparse Odometry’, *IEEE Trans Pattern Anal Mach Intell*, vol. 40, no. 3, pp. 611–625, Mar. 2018, doi: 10.1109/TPAMI.2017.2658577.
- [6] T. Qin, P. Li, and S. Shen, ‘VINS-Mono: A Robust and Versatile Monocular Visual-Inertial State Estimator’, *IEEE Transactions on Robotics*, vol. 34, no. 4, pp. 1004–1020, Aug. 2018, doi: 10.1109/TRO.2018.2853729.
- [7] A. Rosinol, M. Abate, Y. Chang, and L. Carlone, ‘Kimera: an Open-Source Library for Real-Time Metric-Semantic Localization and Mapping’. [Online]. Available: <https://github.com/MIT-SPARK/Kimera>
- [8] G. Huang, ‘Visual-Inertial Navigation: A Concise Review’, Jun. 2019, [Online]. Available: <http://arxiv.org/abs/1906.02650>
- [9] M. Bloesch, M. Burri, S. Omari, M. Hutter, and R. Siegwart, ‘Iterated extended Kalman filter based visual-inertial odometry using direct photometric feedback’, *International Journal of Robotics Research*, vol. 36, no. 10, pp. 1053–1072, Sep. 2017, doi: 10.1177/0278364917728574.
- [10] M. Brossard, S. Bonnabel, and A. Barrau, ‘Invariant Kalman Filtering for Visual Inertial SLAM’, in *2018 21st International Conference on Information Fusion (FUSION)*, Jul. 2018, pp. 2021–2028. doi: 10.23919/ICIF.2018.8455807.
- [11] J. Delmerico and D. Scaramuzza, ‘A Benchmark Comparison of Monocular Visual-Inertial Odometry Algorithms for Flying Robots’, *IEEE International Conference on Robotics and Automation (ICRA)*, 2018.
- [12] A. I. Mourikis and S. I. Roumeliotis, ‘A Multi-State Constraint Kalman Filter for Vision-aided Inertial Navigation’, *ICRA*, vol. 2, p. 6, 2007.
- [13] X. Zheng, Z. Moratto, M. Li, and A. I. Mourikis, ‘Photometric patch-based visual-inertial odometry’, in *Proceedings - IEEE International Conference on Robotics and Automation*, Jul. 2017, pp. 3264–3271. doi: 10.1109/ICRA.2017.7989372.
- [14] S. Heo, J. Cha, and C. G. Park, ‘EKF-Based Visual Inertial Navigation Using Sliding Window Nonlinear Optimization’, *IEEE Transactions on Intelligent Transportation Systems*, vol. 20, no. 7, pp. 2470–2479, Jul. 2019, doi: 10.1109/TITS.2018.2866637.
- [15] K. Sun *et al.*, ‘Robust Stereo Visual Inertial Odometry for Fast Autonomous Flight’, *IEEE Robot Autom Lett*, vol. 3, no. 2, pp. 965–972, Apr. 2018, doi: 10.1109/LRA.2018.2793349.
- [16] J. A. Hesch, D. G. Kottas, S. L. Bowman, and S. I. Roumeliotis, ‘Consistency Analysis and Improvement of Vision-aided Inertial Navigation’, *IEEE Transactions on Robotics*, vol. 30, no. 1, pp. 158–176, Feb. 2014, doi: 10.1109/TRO.2013.2277549.
- [17] G. P. Huang, A. I. Mourikis, and S. I. Roumeliotis, ‘A First-Estimates Jacobian EKF for Improving SLAM Consistency’, 2009, pp. 373–382. doi: 10.1007/978-3-642-00196-3_43.
- [18] F. Ma, J. Shi, Y. Yang, J. Li, and K. Dai, ‘ACK-MSCKF: Tightly-Coupled Ackermann Multi-State Constraint Kalman Filter for Autonomous Vehicle Localization’, *Sensors*, vol. 19, no. 21, p. 4816, Nov. 2019, doi: 10.3390/s19214816.
- [19] C. Chen, B. Wang, C. X. Lu, N. Trigoni, and A. Markham, ‘A Survey on Deep Learning for Localization and Mapping: Towards the Age of Spatial Machine Intelligence’, Jun. 2020, [Online]. Available: <http://arxiv.org/abs/2006.12567>
- [20] C. Li and S. L. Waslander, ‘Towards End-to-end Learning of Visual Inertial Odometry with an EKF’. [Online]. Available: <https://github.com/lichunshang/deep>
- [21] X. Zuo, N. Merrill, W. Li, Y. Liu, M. Pollefeys, and G. Huang, ‘CodeVIO: Visual-Inertial Odometry with Learned Optimizable Dense Depth’, Oct. 2021, pp. 14382–14388. doi: 10.1109/icra48506.2021.9560792.
- [22] B. Triggs, P. F. McLauchlan, R. I. Hartley, and A. W. Fitzgibbon, ‘Bundle Adjustment — A Modern Synthesis’, 2000, pp. 298–372. doi: 10.1007/3-540-44480-7_21.
- [23] S. Nousias and C. Bergeles, ‘Large-Scale, Metric Structure from Motion for Unordered Light Fields’, *Proceedings of the IEEE/CVF Conference on Computer Vision and Pattern Recognition*, pp. 3292–3301, 2019.
- [24] M. Burri *et al.*, ‘The EuRoC micro aerial vehicle datasets’, *Int J Rob Res*, vol. 35, no. 10, pp. 1157–1163, Sep. 2016, doi: 10.1177/0278364915620033.
- [25] C. Tomasi and T. Kanade, ‘Shape and Motion from Image Streams: a Factorization Method|Part 3 Detection and Tracking of Point Features’, 1991.
- [26] J. D. Foley, M. A. Fischler, and R. C. Bolles, ‘Graphics and Image Processing Random Sample Consensus: A Paradigm for Model Fitting with Applications to Image Analysis and Automated Cartography’, 1981.
- [27] C. Forster, Z. Zhang, M. Gassner, M. Werlberger, and D. Scaramuzza, ‘SVO: Semi-Direct Visual Odometry for Monocular and Multi-Camera Systems’, *IEEE Transactions on Robotics*, vol. 33, pp. 249–265, 2016, [Online]. Available: <https://youtu.be/hR8uq1RTUfA>

> REPLACE THIS LINE WITH YOUR MANUSCRIPT ID NUMBER (DOUBLE-CLICK HERE TO EDIT) <

- [28] M. Li and A. I. Mourikis, 'High-precision, consistent EKF-based visual-inertial odometry', *Int J Rob Res*, vol. 32, no. 6, pp. 690–711, May 2013, doi: 10.1177/0278364913481251.
- [29] J. and N. J. and S. T. and H. T. and S. R. Rehder, 'Extending kalibr: Calibrating the extrinsics of multiple IMUs and of individual axes', *IEEE International Conference on Robotics and Automation (ICRA)*, 2016.